Manuscript prepared for Atmos. Chem. Phys. Discuss.
with version 2014/05/30 6.91 Copernicus papers of the LaTeX class copernicus.cls.
Date: 11 May 2015

Using IASI to Simulate the Total Spectrum of Outgoing Longwave Radiances

Emma C. Turner[1], **Hai-Tien Lee**[2], **and Simon F. B. Tett**[1]

[1]School of Geosciences, University of Edinburgh, UK
[2]Earth System Science Interdisciplinary Center, University of Maryland, College Park, Maryland, USA

Correspondence to: Emma Turner
(et384@cam.ac.uk)

Abstract

A new method of deriving high-resolution top-of-atmosphere spectral radiances in 10181 bands, over the whole outgoing longwave spectrum of the Earth, is presented. Correlations between different channels measured by the Infrared Atmospheric Sounding Interfermeter (IASI) on the MetOp-A satellite and unobserved wavenumbers are used to estimate far infrared radiances at 0.5 cm^{-1} intervals between 25.25 - 644.75 cm^{-1} (the far infrared), and additionally between 2760 - 3000 cm^{-1}. Radiances simulated by the Line-By-Line Radiative Transfer Model (LBLRTM) with are used to construct the prediction model. The spectrum is validated by comparing the Integrated Nadir Longwave Radiance (INLR) product spanning the whole 25.25 - 3000 cm^{-1} range with the corresponding broadband measurements from the Clouds and the Earth's Radiant Energy System (CERES) instrument on the Terra and Aqua satellites at points of simultaneous nadir overpass. This has mean differences of 0.3 $Wm^{-2}sr^{-1}$ (a 0.5% relative difference). This is well within the uncertainties associated with the measurements made by either instruments. However, there is a noticeable contrast when the bias is separated into night and daytime scenes with the latter being significantly larger, possibly due to errors in the CERES Ed3 SRF correction method. In the absence of an operational spaceborne instrument that isolates the far infrared this product provides a useful proxy for such measurements, within the limits of the regression model it is based on, which is shown to have very low root mean squared errors. The new high resolution spectrum is presented for global mean clear and all skies where the far infrared is shown to contribute 44% and 47% to the total INLR respectively. In terms of the spectral cloud effect (CINLR), the FIR contributes 19% and in some subtropical instances appears to be negative, results that would go un-observed with a traditional broadband analysis.

1 Introduction

Because different thermal wavelengths are sensitive to different atmospheric components, remotely sensed hyperspectral and narrowband radiance measurements contain valuable information about atmospheric, surface and cloud properties, and also reveal fingerprints of long-term

climate trends (Harries et al., 2001). Additionally they have a unique value in evaluating climate models (Goody et al., 1998). As such there is a need for detailed and complete satellite observations of terrestrial outgoing longwave radiation (OLR) in the 25 - 3000 cm^{-1} wavenumber range (3 - 400 μm wavelength) at the spectral level (Anderson et al., 2004). At the present time, however, there is no satellite instrument in operation that isolates a substantial part of the OLR with the longest wavelengths, known as the Far Infrared (FIR).

The FIR, which we define as those wavenumbers between 25 - 650 cm^{-1} (15 - 400 μm), is modulated by water vapour absorption in the pure rotation band and, to a lesser extent, the water vapour continuum. For the all-sky Harries et al. (2008) estimate that about 45% of the total OLR from the Earth is from the FIR. Although individual transitions in this region are low in energy, because rotational transitions are lower in characteristic frequency than vibrational transitions, the combined intensity of outgoing radiance at these wavelengths is large. The abundance of water vapour in the troposphere strongly absorbs most of the FIR that originates from the surface meaning that, apart from over some very dry and cold regions, the majority that reaches the TOA is emitted from the upper troposphere. Satellite measurements in this wavelength range would be a rich source of information about upper tropospheric water vapour (Mlynczak et al., 2004; Huang et al., 2007), its continuum absorption (Green et al., 2012), the radiative influence of cirrus clouds (Rizzi and Mannozzi, 2000; Maestri and Rizzi, 2003; Wang et al., 2014), as well as providing unique information for climate model validation.

Current operational space borne hyperspectral sounders such as the Atmospheric Infrared Sounder (AIRS) (Chahine et al., 2006) or the Infrared Atmospheric Sounding Interfermeter (IASI) (Blumstein et al., 2004) have been designed to measure only the mid infrared part of the OLR. Photons at FIR frequencies have lower energies than typical band gap energies so suitable photodiodes are difficult to make. Mercury Cadmium Telluride (HgCdTe) detectors such as those used within the IASI instrument can be designed for lower frequencies, however a 650 cm^{-1} cut off is common due to the enhanced sensitivity required to measure below this threshold. In order to maintain the high signal to noise ratio the detector needs to be cooled significantly to reduce the number of photons generated by the detector itself and achieve the precision required. Microwave satellite detectors such as the Microwave Limb Sounder (MLS)

or the Advanced Microwave Sounding Unit (AMSU) sense wavelengths that are just longer than the FIR. However, they use very different radiance measurement technologies. Both of these restrictions from either side of the FIR result in an unmeasured segment of electromagnetic radiation that has generally only been observed as part of the total infrared radiation by broadband devices.

Currently the only spaceborne instrument to spectrally resolve part of the FIR has been the Infrared Interferometer Spectrometer (IRIS) which flew onboard the Nimbus 3 and Nimbus 4 satellites in 1969 and 1970 respectively (Hanel et al., 1972). It had a maximum wavenumber of 400 cm^{-1} (25 μm) and a spectral resolution of 2.8 cm^{-1}. Since then, a limited number of instruments have been developed to measure part of, or all of, the FIR. Some have been part of balloon-borne and ground-based campaigns, such as the Atmospheric Emitted Radiance Interferometer (AERI) (Turner et al., 2004), and the Radiation Explorer in the Far InfraRed (REFIR-BB/PAD) (Esposito et al., 2007), whose measurements have been used to test the representation of the FIR by line-by-line radiative transfer models (Bianchini et al., 2008). Aircraft campaigns using instruments such as the Tropospheric Airborne Fourier Transform Spectrometer (TAFTS) Green et al. (2012), REFIR-PAD (Palchetti et al., 2008), and the Interferometer for Basic Observation of Emitted Spectral Radiance of the Troposphere (I-BEST) Masiello et al. (2012), have been used to gain insights into the FIR continuum. Though these airborne experiments do prove useful for testing parametrisations in radiative transfer models, only spaceborne instruments can give the full Earth coverage of sufficient temporal length needed for climate studies.

Recently, much work has been put into developing and testing a detector proposed for a spaceborne mission with a response in the 50 - 2000 cm^{-1} range at high spectral resolution (approximately 0.643 cm^{-1}). The Far-Infrared Spectroscopy of the Troposphere (FIRST) instrument (Mlynczak et al., 2004) has detectors that are cooled to 4.2K with liquid helium to achieve the necessary sensitivity (for comparison the optical core of IASI is 91.3K). Initial comparisons of FIRST measurements taken on balloon flights against theoretical calculations and spectral overlaps with coincident satellite instruments show excellent fidelity (Mlynczak et al., 2006). However, despite high priority recommendations (see Board et al. (2007)) there is currently

no scheduled launch date for its deployment, even though it is often noted that the FIR has been measured extensively and directly on every planet in the solar system except Earth (Hanel, 2003).

Historically, when parts of the infrared spectrum are unmeasured from space the remaining bands have often estimated through alternate means. Previous studies have sought to reproduce total OLR from narrowband and hyperspectral sounders with the combined motivations of validating current operational broadband sounders, mitigating them against potential failure and gaining wider diurnal coverage. The absence of an instrument that measured total outgoing LW flux in the 1970's led to its estimation using a single waveband in the 800 - 950 cm^{-1} window region (10.5 - 12.5μm) from the two-channel scanning radiometer onboard the NOAA-1 to NOAA-5 satellite platforms via a non-linear regression model derived from radiative transfer calculations applied to 99 different atmospheric profiles (Gruber, 1977; Gruber and Winston, 1978). As the reference broadband results are obtained from a radiative transfer code this method is termed 'theoretical'. Alternatively, Ohring et al. (1984) used the Earth Radiation Budget (ERB) broadband OLR measurements on the Nimbus 7 satellite as a reference to obtain regression coefficients between these and window band observations from the Temperature Humidity Infrared Radiometer (THIR) instrument on the same satellite at collocated footprints. This method is termed 'empirical', because actual measured data is used as a reference.

There are uncertainties involved in using only one narrow band to estimate the entire OLR because the atmospheric information contained in one spectral region is limited, eg. see Gruber et al. (1994). An early theoretical OLR product derived with a multi-spectral regression technique used the 4 infrared channels from the Medium Resolution Infrared Radiometer (MRIR) on the Nimbus-3 satellite (Raschke et al., 1973). This method has been adapted for use with the High Resolution Infrared Sounder (HIRS) instruments that have been operational since 1978, thus providing a continuous longterm surrogate for total OLR (Ellingson et al., 1989a). The product has been continuously developed since its creation and has demonstrated extremely high correlations with CERES broadband data (Lee et al., 2007). Recently, Sun et al. (2010) have used the empirical approach to derive broadband data from AIRS using the CERES out-

going LW flux to generate regression coefficients from principal component analysis of AIRS radiances.

Traditionally, these methods employ data from instruments that fly on polar orbiting satellites which are beneficial for global climate studies in terms of their high spatial coverage. However, as they are restricted to monitoring each subsatellite point just twice a day they fall short of the requirements for diurnal analyses. Geostationary satellites, on the other hand, complete a full Earth scan in approximately 30 minutes thus capturing the daily variability, but are restricted to one nadir location with views at increasingly unfavourable angles away from the subsatellite point. Gube (1982) was the first to use geostationary radiances from the 2 infrared channels (10.2 - 13 μm and 5.7 - 7.5 μm) on the METEOSAT-1 satellite to estimate total OLR flux theoretically. Schmetz and Liu (1988) modified this approach using METEOSAT-2 data to include a better treatment of limb-darkening using the method developed by Abel and Gruber (1979), and Cheruy et al. (1991) calculated the relationship between METEOSAT-2 data and collocated footprints from broadband Earth Radiation Budget Experiment (ERBE) measurements to produce empirical regression coefficients. The Geostationary Operational Environment Satellite 6 (GOES-6) Imager window channel (10.2 - 12.2 μm) has also been employed in an empirical estimation of OLR fluxes using ERBE data (Minnis et al., 1991), and Lee et al. (2004) blended HIRS OLR fluxes from polar satellites with GOES-8 Imager data to provide OLR data to incorporate multi-spectral information on temperature and humidity at different elevations, with wider diurnal coverage.

The body of work that exists surrounding the derivation of broadband OLR from narrowband mid infrared measurements is extensive and on-going, however, as regards spectrally resolved measurements in the FIR, progress is limited to a handful of studies. Huang et al. (2006) use clear-sky radiances from the IRIS instrument to predict fluxes in its uncovered spectral regions below 400 cm^{-1} and above 1400 cm^{-1} by assuming a linear relationship between these regions and fluxes in the H_2O ν_2 band and a narrow window region. Regression coefficients between measured and unmeasured wavebands are obtained from calculated radiances using the MODTRAN radiative transfer model applied to simulated profiles from the GFDL AM2 global climate model. These coefficients are then applied to IRIS to simulate the whole OLR.

Huang et al. (2008) adapt this theoretical method for the hyperspectral Atmospheric Infrared Sounder (AIRS) to derive spectral fluxes in its uncovered wavebands using principle component analysis. A complete set of clear-sky fluxes from 10 to 2000 cm^{-1} are calculated at 10 cm^{-1} intervals, and validated with broadband observations using collocated CERES data for the tropical oceans. Corresponding studies were carried out for cloudy data (Huang et al., 2010), and additional years (Huang et al., 2013). Chen et al. (2013) extend this work to include land and extra-tropical ocean regions using clear-sky data and Huang et al. (2014) build upon this by using all-sky data and calculating spectral cloud radiative effects.

In lieu of complete FIR observations we follow a theoretical approach and develop an algorithm to 'fill in the gaps' of the available data, but with a spectral resolution and range of estimated wavenumbers that is an advance on previous studies. To do this we use the IASI instrument which measures in the mid infrared, originally designed to fulfil both meteorology requirements of high spatial coverage, and atmospheric chemistry needs such as accuracy and detailed vertical resolution (Clerbaux et al., 2009). IASI has 4 times as many channels as the AIRS instrument for the same range of thermal infrared wavelengths, and is free from gaps over the whole spectral range. It is part of the payload of the MetOp-A satellite, which provides a differently timed polar orbit and hence a different sampling of the diurnal cycle to existing satellites that carry broadband instruments. In the absence of any current spaceborne instrument that isolate the FIR our new algorithm has the potential to provide valuable proxy measurements, within the limitations of the spectroscopy implemented in the radiative transfer code used to construct the prediction model. To ensure high accuracy we use the Line-By-Line Radiative Transfer Model (LBLRTM) (Clough et al., 1992, 2005) available publicly at http://rtweb.aer.com, which has a long and successful heritage of being at the leading edge of the field, is continually updated and has been well validated, see for example (Shephard et al., 2009; Delamere et al., 2010; Alvarado et al., 2013). This approach extends existing observations into the far and near infrared using physical knowledge of atmospheric radiative transfer provided by LBLRTM, which we then evaluate using broadband observations from the CERES satellite instrument.

This study differs from most of its associated predecessors by remaining in the directional radiance regime, with no attempt made to translate unfiltered IASI radiances or the total integrated OLR product to flux densities at this stage. Flux is calculated by integrating the measured radiance over all solid angles, which can be split into zenith and azimuth angles. The outgoing radiation field is strongly anisotropic and must be estimated using a predetermined model, of which many exist involving varying degrees of sophistication and assumptions. These can be either theoretically determined using radiative transfer model calculations of flux or empirically derived using satellite measurements over several different viewing angles and locations, for example see Clerbaux et al. (2003); Loeb et al. (2003); Kato and Loeb (2005). The resulting Angular Distribution Models (ADMs) relate the radiance measured at a single angle to irradiance estimated over all angles, and as such introduce a further level of uncertainty into the validation, which can be up to 2.3% for recent satellite products (Instantaneous LW TOA flux: see the CERES Terra Edition3A SSF Data Quality Summary). To avoid confusion we use the abbreviation INLR (Integrated Nadir Longwave Radiance) to refer to the extended spectrum of IASI radiances that has been integrated over all wavenumbers, and is distinct from OLR which is synonymous with the integrated fluxes. This approach has the advantage of allowing for a cleaner comparison with climate model simulated satellite products, such as those calculated by the Radiative Transfer model for TOVS (RTTOV) (Saunders et al., 2013), which can simulate IASI radiances from vertical profiles of climate variables. The adaption of the methodologies adopted in this study for the additional calculation and evaluation of flux quantities are left for future studies.

We use a theoretical based regression technique similar to the one used to derive OLR from the HIRS instrument based on physical atmospheric profiles which is described in section 2.2. In order to verify the extended IASI spectrum we compare the calculated INLR with broadband CERES instruments on other satellites. Section 2.4 explains how times and locations are identified where the path of MetOp-A crosses those of the Aqua and Terra satellites, both of which carry CERES instruments. By restricting this set further to only nadir looking views the instruments will sense the same atmospheric path at the same time, providing the opportunity

for indirect validation of the new IASI product. Results of this are presented in section 3. Finally the complete constructed IASI spectrum is presented in the remaining sections 4.1, 4.2 and 4.3.

2 Data and Methodology

2.1 IASI Level 1c and Combined Sounding Products Data Set

The IASI Flight Model 2 (FM2) instrument on the sun-synchronous MetOp-A satellite was launched by EUMETSAT in October 2006. It is a 8461 channel passive sounder that measures in the mid infrared spectral region between 645 - 2760 cm^{-1} (3.62 - 15.5 μm) at a 0.25 cm^{-1} sampling interval with no gaps. The apodised level 1c radiances have a 0.5 cm^{-1} resolution. The effective field of view (EFOV) is a 2 x 2 matrix of 4 circular instantaneous fields of view (IFOV) that each have an approximate footprint diameter of 12 km at nadir. There are 30 EFOV per scan line which takes 8 seconds to complete and with a maximum scan angle of 48.3° in the across track direction. In its nominal mode IASI uses a view of an internal blackbody and a deep space view once every scanline to calibrate on-board, as described by Simeoni et al. (2004). It has been demonstrated to have a very low absolute brightness temperature radiometric accuracy of 0.25 K in pre-flight testing, and post launch assessments place the absolute calibration uncertainty at or better than 0.5 K (Larar et al., 2010; Illingworth et al., 2009). For discussion of the spectral structure of the noise see Clerbaux et al. (2009).

We restrict the data to the IFOVs with the smallest satellite zenith angles in order to retain only nadir looking pixels. There are 4 IFOVs with angles less than 1.5° which are indices 57, 58, 63 and 64 in the across track direction which have viewing angles of 1.34°, 1.37°, 1.41°, and 1.39° respectively. Alongside the level 1c radiances clear-sky flags are obtained from the related level 2 combined sounding products to construct an equivalent clear-sky product which is used to show clear/cloudy differences in the mean spectrum in section 4.2. Cloud detection in IASI pixels is performed from a choice of 5 separate tests, involving window channels, AMSU-A, AVHRR and CO_2 slicing, depending on the quality of the input data.

2.2 Method for Estimating Radiances at Unmeasured Wavenumbers from IASI

Strong correlations are found between frequencies in the LW spectra with similar spectroscopic properties. Unmeasured radiances with FIR wavenumbers between 25 and 650 cm^{-1} and those between 2760 and 3000 cm^{-1} (which we will term near infrared (NIR) radiances) can be estimated from IASI observations. For example, FIR wavenumbers in the strong H_2O rotational band at 25.25 cm^{-1} have strong correlations with those in the centre of the 667 cm^{-1} CO_2 and 1533 cm^{-1} H_2O ν_2 bands by virtue of their similar sensitivity to high altitude temperatures (Figure 1). However the 1533 cm^{-1} band is physically more similar to frequencies in the FIR and therefore has comparably larger correlations.

Adapting the simulation methodology of Ellingson et al. (1989a), the Line-By-Line Radiative Transfer Model (LBLRTM) is used to simulate LW spectra over the spectral range 25-3000 cm^{-1} at 0.5 cm^{-1} resolution with radiosonde data from 1596 soundings (Phillips et al., 1988). This dataset was compiled by Dr. Norman Phillips of NOAA/NMC with the purpose of creating a representative sample of the range of conditions found in the atmosphere, and has been demonstrated to be adequate enough to base global models upon, see Ellingson et al. (1989b). The profiles were measured during a two-week winter period and a two-week summer period and continental and maritime locations were sampled equally. The following details from Ellingson et al. (1989a) describe the dataset. Each sounding includes temperature values at 65 different pressure levels extrapolated from 0.1 to 1000 mb and mixing ratios of H_2O and O_3 in the corresponding 64 layers. The soundings were compiled from radiosonde ascents from land and ocean stations between 30° S and 60° N and the soundings were equally divided between tropical (30° S - 30° N) and midlatitude (400 summer and 400 winter) conditions. The O_3 data was chosen to be climatologically consistent with the temperature profiles, and the stratospheric H_2O mixing ratio is assumed to be 3 ppmm. Stations with surface heights above 300 m and profiles with no moisture below 700 mb were not used.

A second set of cloudy simulations was obtained by inserting a cloud into each profile at a particular level (randomly distributed) to give 3200 different conditions, 1600 clear and 1600 cloudy. The water vapour profile was not altered when a cloud layer was included and the clouds

were nearly uniformly distributed in low (950 - 850 mb), middle (675 - 525 mb) and high (400 - 240 mb) layers. Clouds are all considered to have 100% horizontal coverage of the profile. Those with cloud top pressures greater than 450 mb are assumed to be spectrally black whereas the high level clouds are assumed to have the spectral properties of cirrus given by Haurwitz and Kuhn (1974). Surface emissivities are assumed as unity (black-body) for all wavenumbers and surface types. Recent studies have shown this is not an accurate assumption as emissivity varies spectrally and with surface type (Feldman et al., 2014), however, over much of globe the FIR itself measured from the TOA contains little contribution from the surface due to the strong water vapour absorption. The channels that best estimate this part of spectrum will have similar physical properties and hence are around the water vapour ν_2 band (see Figure 3a), which is also highly opaque to the surface in the regions where the radiosonde data was taken. However, for those channels in the near and mid infrared, or in 'micro windows', this assumption will have an impact upon results though the combined effect will likely be small. For certain polar scenes, such as over the Antarctic Plateau, differences will be greater because the atmosphere here is high and dry enough to allow more far infrared emission to space from the surface (Chen et al., 2014).

Several regression model formulations were investigated for the purpose of NIR/FIR radiance prediction. A log-log transformation was found to provide the optimal performance in minimization of estimation errors and regression residual distributions. This empirical behaviour can also be explained physically, as transmittances vary with optical path via an exponential relationship and hence the model will be approximately linear. Figure 2 shows an example of the log-log relationship between radiances at 33.75 cm^{-1} and the channel that has a maximum correlation with it (2091.25 cm^{-1}).

The best predictor channels are selected as those with maximum correlation coefficients between the log-radiances (Figure 3) whose values are shown in Figure 4. For this application the local zenith angle is restricted to the nadir cases. The prediction equation to estimate the radiance $I_{\nu_{FIR/NIR}}$ in either the FIR or NIR regions at wavenumber ν can be written as,

$$\ln(I_{\nu_{FIR/NIR}}) = a_0 + a_1 \ln(I_{\nu_{predictor}}) \quad (1)$$

where $I_{\nu_{predictor}}$ is the radiance observed by IASI at the predictor wavenumber ($Wm^{-2}sr^{-1}(cm^{-1})^{-1}$) and a_0 and a_1 are the calculated regression coefficients. The mean spectral radiance calculated by LBLRTM for each wavenumber in the FIR is shown in the left panel of Figure 5 and has a total integrated value of 36.32 $Wm^{-2}sr^{-1}$. The corresponding value for the NIR region is 0.028 $Wm^{-2}sr^{-1}$ (6). The root mean square (rms) errors in the regression model serves as the theoretical estimates for the reconstruction uncertainties in the reconstructed spectrum, shown in the right panels of Figures 5 and 6. The root mean square of the summed radiance errors, including cancellations from positive and negative values, is 0.054 $Wm^{-2}sr^{-1}$ over all simulated regions which gives a total relative error of 0.15%. For comparison radiometric noise from IASI is below 10^{-5} $W^{-2}sr^{-1}cm^{-1}$ for individual channels (Fig. 2 of Clerbaux et al. (2009)) Individual root mean square relative errors are shown in Figure 7 which shows a very low dependency on wavenumber for the FIR region, most of which do not exceed 1%, with higher relative errors seen in the extreme NIR due to low absolute values.

2.3 CERES Single Scanner Footprint (SSF) Ed3A

The INLR product constructed from the extended IASI radiances is compared with the existing CERES directional radiance product. The CERES SSF Edition 3A dataset is obtained from the Atmospheric Science Data Center at the NASA Langley Research Center for both the Terra and Aqua polar orbiting satellites (Wielicki et al., 1996). In the cross-track scanning mode there are 90 FOVs in a single scanline with a 25 km footprint at nadir, however in terms of measurements and products it usually considered at a resolution of about 20 km. The swath takes 6.6 seconds to complete and has a maximum scan angle of 65.8°. For the present study only pixels with the minimum satellite zenith angles, which are less than 1° (FOV 45 and 46) are selected to retain only nadir-looking views. Each satellite carries 2 identical CERES instruments. For the data acquired, Flight Model 1 (FM1) on Terra and Flight Model 3 (FM3) on Aqua are operational in the cross-track mode.

Cloud properties for CERES instruments are inferred from the Moderate-Resolution Imaging Spectroradiometer (MODIS) imager which flies on the same satellites, and are based on threshold tests with adjacent channels (Minnis et al., 2004). Clear and cloudy scenes are identified

using the near infrared 3.7 μm channel on MODIS. Single channel retrieval of cloud properties has its weaknesses, however, the 3.7 μm channel is recommended for most cloud applications because of its greater sensitivity to thin cloud-top microstructure and because it is less affected by surface contamination than its neighbouring 1.6 μm channel, for example (Rosenfeld et al., 2004). A recent comparison of MODIS retrievals with in situ data also revealed that the 3.7 μm channel displays the best agreement (King et al., 2013). A threshold clear fraction of greater than 80% is chosen to partition clear pixels.

CERES measures filtered radiances in terms of physical origin (i.e. thermal or solar), rather than imposing wavelength boundaries, however approximate ranges for the 3 channels are reflected shortwave (SW) (0.3 - 5 μm), total (0.3 - 200 μm), and window (8 - 12 μm). LW radiation is determined from a weighted combination of measurements from the other channels and hence all emitted thermal radiances that fall within the 0.3 - 200 μm (50 - >3000 cm^{-1}) range are included.

Relative errors due to the process of unfiltering radiances are found to be generally less than 0.2% in the LW (Loeb et al., 2001). The uncertainty in net TOA flux due to absolute calibration uncertainty including the radiance-to-flux conversion is 2% in the SW channel and 1% in the total channel at the 95% confidence level (Priestley et al., 2002). Since nighttime LW radiation is based only on the total channel the uncertainties are essentially the same at 1%. For the daytime combining the uncertainties of the SW channel yields an estimate of around 2.1%, which produces an average daily LW uncertainty of 1.5% (see appendix of Loeb et al. (2009) for the derivation). Given that the the present study uses CERES unfiltered radiances only, contributed uncertainties from the radiance-to-flux conversion do not apply, but as these errors are unknown the total level of uncertainty has an upper bound of about 1.5%.

Determining absolute radiometric calibration uncertainty once in-orbit is dependent on a reference instrument and it remains a challenge to achieve a reference traceable to international standards. This is a problem of such critical importance that it led to the formation of an international effort called the Global Space-Based Intercalibration System (GSICS) (Goldberg et al., 2011). The current CERES Edition-3 product established FM1 as the reference to place all the CERES instruments of the same radiometric scale and as such will contain fewer correction

uncertainties. All flight models were corrected for spectral darkening at shorter wavelengths (<1 μm) due to UV exposure which caused degradation in both the SW channel and the shorter wavelength region of the total sensors. Studies that use an edition of CERES prior to Edition 3 will be subject to this error, which overestimates flux by as much as a 0.8% (CERES LW flux daytime for FM1 and FM3: see the CERES Terra and Aqua Edition3A SSF Data Quality Summary). Further refinements for the spectral correction have been proposed for the CERES Edition 4 production (Thomas and Priestley, 2014). This revision is expected to improve the accuracy and stability of CERES data, particularly over the daytime land scenes. The present study uses CERES Edition 3 data and as such, it is important to be aware of the possible errors relating to this version.

2.4 Identifying Simultaneous Nadir Overpasses

Two satellites in sun-synchronous polar orbits with different equatorial crossing times will cross in the polar regions at approximately the same north/south latitude each time. When radiometers from both satellites view the same nadir scene at the same time this is called a simultaneous nadir overpass (SNO). Using SNOs is preferable to comparing composite measurements over the same time period because individual scene differences between cloud and surface properties are avoided. This study uses the database of predicted SNOs provided by the National Calibration Center of NOAA; available at http://ncc.nesdis.noaa.gov/SNO/SNOs//NCC_SNOs_prediction_service.html which makes SNO predictions based on the SGP4 orbital perturbation model (Cao et al., 2004).

Aqua has local equatorial crossing times (LECTs) of 13.30 (ascending) and 01.30 (descending), and Terra has LECTs of 22.30 (ascending) and 10.30 (descending). MetOp-A has an ascending node of 21:30 and a descending node LECT of 09:30. 2012 SNOs between MetOp-A and Aqua, and MetOp-A and Terra, are first filtered following the criteria set out in the methodology of Cao et al. (2005). This specifies that at the SNO: 1) the time difference between nadir pixels is less than 30 seconds and, (2) the distance between nadir pixels is less than the diameter of one footprint. Based on the average of the 20 km CERES pixel and the 12 km IASI pixel this threshold is set to 16 km. This yields approximately 100 SNOs for each satellite pair over the

course of a year. Using the predictions the closest matches in terms of time and distance were identified in the satellite data for the most nadir-looking field of views for each instrument. The resulting locations of IASI pixels identified as SNOs are shown in Figure 8. By virtue of their different equatorial crossing times MetOp-A and Aqua SNOs all lie around 74° N/S and MetOp-A and Terra SNOs all lie around 81° N/S.

3 Validation of INLR at Simultaneous Nadir Overpasses with CERES

For maximum consistency with CERES, IASI INLR radiances are cut off at the 50 cm^{-1} lower wavenumber limit, and integrated over all remaining radiances up to 3000 cm^{-1}. INLR estimates from coincident IASI and CERES pixels generally lie close together, with the majority falling within 2 $Wm^{-2}sr^{-1}$ of each other (Figure 9). In general differences will be introduced by the slightly different nadir angles and footprint sizes between CERES and IASI, and the accuracy of the colocations. Absolute values range from 30 to over 80 $Wm^{-2}sr^{-1}$ yet there is no identifiable relationship between scene radiance and bias indicating our algorithm is robust against profile conditions at these latitudes. Nighttime radiances show a slightly higher correlation (0.99) compared with daytime scenes (0.98). Whether the lower daytime correlation originates from errors in the SW channel involved in estimating daytime CERES radiances, solar backscatter contamination of either instrument or the increased variability of daytime radiances is beyond the scope of this study.

The same results shown as absolute biases (CERES - IASI) are presented as a time series in Figure 10, revealing no dependency of error upon season. Table 1 breaks down these biases by CERES instrument. Mean IASI INLR values are about 0.3 $Wm^{-2}sr^{-1}$ lower than CERES when all local times are considered, and individual differences are generally within ± 6 $Wm^{-2}sr^{-1}$. When split into clear and cloudy scenes, (Figure 11), it is evident that these larger biases are associated with partly cloudy or overcast scenes and are likely due to horizontal cloud inhomogeneity in the region of the SNO which can have a large effect on the height, and hence temperature/radiance of emission. Though this results in a larger standard deviation for all cloudy scenes the mean clear and cloudy biases are very similar, with a difference of 0.04 $Wm^{-2}sr^{-1}$)

between them, suggesting our algorithm is robust against this division of scenes. However, developing scene dependent coefficients is a feature that could be added in the future to further improve the method's performance, combined with an enhanced treatment of different cloud types, such as cirrus, within the radiative transfer code.

When relative differences are considered LW radiances are about 0.5% higher in CERES than IASI overall (Table 1). Split into day and nighttime scenes it is apparent that this bias is dominated by daytime pixels as the mean nighttime relative error is only 0.01% whereas daytime differences are 0.95%. Higher biases are seen in the daytime relative to nighttime across all scene types and platforms and are calculated to be statistically significantly different from zero, indicating a systematic bias which could be related to the CERES Ed4 findings about the SRF correction determination method described in section 2.3.

All relative differences are well within the uncertainty range of CERES unfiltered radiance based on absolute radiometric calibration uncertainty and relative unfiltering errors as detailed in section 2.3. Given that the original correlation co-efficients between radiances were calculated using only tropical and mid-latitude profiles, the fact that the algorithm performs well in polar regions shows that it is robust under different scene types, however, maximum accuracy would be achieved by developing separate algorithms for appropriate subsets.

4 Extended IASI Spectral Nadir Radiances

4.1 Instantaneous Spectrum

Example extended instantaneous IASI radiance spectra from 17th April 2012 show that the estimated FIR contributes between 42 - 64% to the total INLR depending on the scene type (Figure 12). This is within the range of previous estimates (Harries et al., 2008). We present night time scenes which is when the FIR is particularly dominant as temperatures fall. In the daytime, however, higher surface temperatures often allow the window region to reach higher intensities when there is little or no cloud (Lindfors et al., 2011). In non-cloudy cases temperature is the dominating factor controlling the total intensity of LW radiance received at the TOA.

For example, the spectrum over the Sahara (Figure 12c) emits about double the total radiance as that over Antarctica (Figure 12d). However when clouds are present their height and coverage can have a highly significant influence. For example it is certain that the temperature in the tropics will be higher than that in Antarctica, and yet Figure 12a and Figure 12d have similar values of total INLR. This is because it is likely that deep convective cloud brings the height of tropical emission to the cold upper troposphere where photons have lower energies. Clouds give more weight to the FIR as part of the INLR overall. The desert and the tropics are both warm regions and yet the FIR contributes 42% of the former clear dry case and 62% of the latter moist cloudy case, which is almost a third greater. The low stratiform clouds that are prevalent over midlatitude land will not have as large an effect on the whole spectrum (Figure 12b), but emission in the window region is still reduced with respect to the FIR.

4.2 Mean Clear and Cloudy Spectrum

When split into global mean clear and cloudy scenes an average of 47% of the total LW radiance comes from wavenumbers less than 645 cm^{-1} when clouds are present, and 44% when the atmospheric column is clear (Figure 13a). The peak wavelength of emission also shifts from 558.25 to 513.25 cm^{-1} in the cloudy only case. The NIR region constructed from a similar method contributes near-negligible radiances of 0.03 $Wm^{-2}sr^{-1}$ (0.04%) in cloudy cases and 0.05 $Wm^{-2}sr^{-1}$ (0.06%) in clear cases. This is a region of partial transparency and hence like the 800 - 1250 cm^{-1} window is more important in the clear-sky.

The difference between the averaged clear and all-sky is equivalent to the cloud effect and using flux quantities this is often know as the cloud radiative forcing (CRF) or the cloud radiative effect (CRE). By analogy we use the term 'Cloud Integrated Nadir Longwave Radiance' (CINLR) to refer to the radiance equivalent of CRF. Figure 13b shows this radiance equivalent cloud effect for the whole LW spectrum, with a total CINLR value of 8.1 $Wm^{-2}sr^{-1}$. In general there is more outgoing radiation at all wavenumbers in the clear-sky because liquid clouds are nearly opaque to the whole infrared radiance spectrum and re-emit at lower temperatures/energies than the clear-sky case. Wavebands at 0 - 200 cm^{-1}, 650 - 700 cm^{-1}, and around 1500 cm^{-1}, are strongly sensitive to rotational water vapour transitions, CO_2 ν_2 transitions, and

the vibrational ν_2 water vapour transitions respectively. As such peak emissions are in the upper troposphere/lower stratosphere where clouds are few and hence the CINLR is low. Even though in the cloudy case the FIR represents a more significant proportion of the total INLR, the clear-sky still emits more over this wavelength range in terms of absolute magnitude. Although the majority of the energy in the CINLR is distributed over the atmospheric window spectral interval, the FIR still accounts for 19% of the total CINLR.

4.3 Maps of INLR, FIR and window wavebands

Spatially, all-sky IASI INLR averaged over the whole month of April 2012 peaks in the clear desert and extra-tropical subsidence regions around $\pm 20^\circ$. In the latter low maritime clouds emit radiation at high temperatures similar to those at the surface (Figure 14a). Deep convective clouds over the intertropical convergence zone, Indo-Pacific warm pool and monsoon regions of Africa and South America reduce INLR because emission is from high, cold cirrus cloud tops. Correspondingly these regions also have the highest CINLR values (Figure 14b), as the difference between the all and the clear-sky is at a maximum. An interesting feature of this plot are occasional negative CINLR values, bordering the polar continents. These values tend not to be lower than -1 $Wm^{-2}sr^{-1}$. CINLR is generally a positive quantity, i.e. if a cloud is added to any particular clear-sky scene instantaneously the radiation emitted from the top of the cloud will be reduced with respect to the clear-sky amount. However, when a lower tropospheric temperature inversion is present, clouds can be warmer than the surface. These clouds are particularly common over the Antarctic Plateau in austral winter as a result of the snow-surface emissivity being greater than the atmospheric emissivity. Additionally cloud detection algorithms often struggle in the polar regions due to lack of thermal contrast between ice covered surfaces and cloud tops. Temperature inversions are also a prominent feature of the subtropical trade wind regimes produced by the subsiding air masses in the descending branches of the Hadley and Ferrel cells. As the mass descends the pressure increases and its volume decreases adiabatically, and hence as the energy is unable to be dissipated as heat its temperature rises warming the air and producing shallow cumulus clouds with a higher temperature than the surface. Examples of this behaviour are visible in the data around $\pm 20^\circ$ in Figure 14b.

The proportion of the radiance spectrum that falls within the FIR waveband peaks in the coldest latitudes of Antarctica as most of the outgoing photons have very low energies and hence low wavenumbers (Figure 14c). It is also higher in regions of greater cloud cover, and this can be identified in the deep convective cloud regions with respect to the surrounding clearer areas, such as over the Sahara. The FIR and the window (WIN) waveband between 800 and 1250 cm^{-1} (Figure 14e) are inverse to one another in terms of zonal variability, i.e. when the FIR contribution is higher the WIN contribution is lower and vice versa. However, the FIR contributes an average of 40% more that the WIN to the INLR overall in terms of absolute magnitude. In terms of contribution to the CINLR though, the WIN is 3 times greater on average than the FIR (Figure 14d and f), but again the patterns of zonal variability are inverse to each other. Interestingly, in the subtropical subsidence regions there are some negative values of CINLR in the FIR, meaning the average all-sky radiation is more than the average clear-sky at these wavenumbers. As the total INLR and the WIN CINLR are still positive in (most of) these locations these cannot be attributed solely to temperature inversions. It is possible to speculate about the cause of this behaviour, for example, clear skies associated with humid conditions and trade wind inversion clouds associated with dryer conditions would result in a higher emission level for the FIR. The dissipation of marine boundary layer clouds resulting in moister clear areas surrounding dryer cloudy areas is a phenomena that has been observed by previous studies (Sohn and Bennartz, 2008), and is something that could be verified by IASI humidity retrievals in future work. As a result of these negative FIR CINLRs, the corresponding positive WIN CINLRs peak at these locations because they are now contributing more to the positive total INLR CINLR. This value is still low due to these two parts of the spectrum cancelling with one another, something that would go un-observed with a purely broadband analysis.

5 Conclusions and Discussion

In this study we have shown that IASI can be used to simulate the entire range of wavenumbers (25 - 3000 cm^{-1}) needed to estimate the total spectrum of outgoing longwave radiances at a sampling resolution of 0.5 cm^{-1} in the far infrared (<645 cm^{-1}) and the near infrared (>2600 cm^{-1}).

The method is based on correlations between measured and un-measured parts of the spectrum, derived using simulations from the Line-By-Line Radiative Transfer Model LBLRTM applied to 3200 measured atmospheric profiles. Broadband observations on other satellite platforms place constraints on the total radiant energy which effectively provides a direct comparison of the simulated regions, assuming the parts of the spectrum where CERES overlaps with IASI are in agreement, within the bounds of uncertainty introduced by calibration differences and other factors. This uncertainty is quantified at an upper limit of 1.5% for LW CERES radiances, and coincident all-sky measurements between IASI and CERES at simultaneous nadir overpasses in polar regions show mean differences of about 0.3 $Wm^{-2}sr^{-1}$ (0.5% relative difference), which is well within this range. This is a strict test of the regression model, given that the two sets of measurements are completely independent and approximately 50% of the INLR is being estimated. However, precise validation of each simulated channel is not possible at the present time and such an assessment would have to be left for the future when space-borne FIR measurements are made available. This study strengthens the case for such an instrument with which to further validate and develop this model on a spectral level.

Instantaneous examples of the simulated spectrum show the far infrared contributes between 43 - 64% to the total Integrated Nadir Longwave Radiance (INLR) with a global weighted average of 47% in the all-sky and 44% in the clear-sky. The results of our comparison are similar to previous values proposed in the literature for the angular integrated flux (45% for the all-sky) Harries et al. (2008), which is interesting considering they are two distinct quantities. This study serves as a proof of concept of the usefulness of IASI for estimating the terrestrial far infrared at an unprecedented level of spectral resolution. Quantities such as cloud radiative forcing which are commonly studied only as a single integrated quantity across the longwave spectrum contain much more information when examined on a spectral level, and in the absence of any corresponding empirical data in the FIR region this product provides a 'next best' alternative.

It is feasible that this product could be developed by applying angular distribution models to the radiances to give flux estimates using a similar approach taken by previous studies (e.g. Huang et al. (2008)), and as such IASI has the potential to be supplement existing broadband instrument observations. The algorithm as it stands is self-contained for all scene types,

however, as anisotropy varies considerably with scene the regression algorithm could be customised to consider cloud cover, surface type and further inhomogeneities. Other inclusions in the construction of the model, such as instrument noise and determination of the optimal spectral interval size for the predictors could additionally refine the models performance further in the future, and as such we consider the model presented herein as a 'first version'. Given that IASI will eventually be carried by 3 different MetOp satellites in the same local-time orbit, and IASI - New Generation proposed for the second generation of MetOp satellites will have even higher sampling resolution (0.125 cm^{-1}) (Crevoisier et al., 2013), this provides the possibility of a product with valuable length and the ability to be inter-satellite calibrated between instruments.

Acknowledgements. CERES and IASI data was provided by NOAA and EUMETSAT respectively. We thank Norman Loeb, Helen Brindley and 3 anonymous reviewers for valuable comments. This work was funded as part of Emma Turner's PhD scholarship by the National Environmental Research Council of the UK.

References

Abel, P. and Gruber, A.: An Improved Model for the Calculation of Longwave Flux at 11 [mu] m, NOAA Tech. Rep. NESS, p. 24, 1979.

Alvarado, M., Payne, V., Mlawer, E., Uymin, G., Shephard, M., Cady-Pereira, K., Delamere, J., and Moncet, J.: Performance of the Line-By-Line Radiative Transfer Model (LBLRTM) for temperature, water vapor, and trace gas retrievals: recent updates evaluated with IASI case studies, Atmos. Chem. Phys, 13, 6687–6711, 2013.

Anderson, J., Dykema, J., Goody, R., Hu, H., and Kirk-Davidoff, D.: Absolute, spectrally-resolved, thermal radiance: a benchmark for climate monitoring from space, Journal of Quantitative Spectroscopy and Radiative Transfer, 85, 367–383, 2004.

Bianchini, G., Carli, B., Cortesi, U., Del Bianco, S., Gai, M., and Palchetti, L.: Test of far-infrared atmospheric spectroscopy using wide-band balloon-borne measurements of the upwelling radiance, Journal of Quantitative Spectroscopy and Radiative Transfer, 109, 1030–1042, 2008.

Blumstein, D., Chalon, G., Carlier, T., Buil, C., Hebert, P., Maciaszek, T., Ponce, G., Phulpin, T., Tournier, B., Simeoni, D., et al.: IASI instrument: Technical overview and measured performances, in:

Optical Science and Technology, the SPIE 49th Annual Meeting, pp. 196–207, International Society for Optics and Photonics, 2004.

Board, S. S. et al.: Earth science and applications from space: National imperatives for the next decade and beyond, National Academies Press, 2007.

Cao, C., Weinreb, M., and Xu, H.: Predicting simultaneous nadir overpasses among polar-orbiting meteorological satellites for the intersatellite calibration of radiometers, Journal of Atmospheric and Oceanic Technology, 21, 537–542, 2004.

Cao, C., Ciren, P., Goldberg, M., and Weng, F.: Intersatellite calibration of HIRS from 1980 to 2003 using the simultaneous nadir overpass (SNO) method for improved consistency and quality of climate data, in: Int. TOVS Study Conf, 2005.

Chahine, M. T., Pagano, T. S., Aumann, H. H., Atlas, R., Barnet, C., Blaisdell, J., Chen, L., Divakarla, M., Fetzer, E. J., Goldberg, M., et al.: AIRS: Improving weather forecasting and providing new data on greenhouse gases., Bulletin of the American Meteorological Society, 87, 2006.

Chen, X., Huang, X., Loeb, N. G., and Wei, H.: Comparisons of Clear-Sky Outgoing Far-IR Flux Infered from Satellite Observations and Computed from the Three Most Recent Reanalysis Products, Journal of Climate, 26, 478–494, 2013.

Chen, X., Huang, X., and Flanner, M. G.: Sensitivity of modeled far-IR radiation budgets in polar continents to treatments of snow surface and ice cloud radiative properties, Geophysical Research Letters, 41, 6530–6537, 2014.

Cheruy, F., Kandel, R., and Duvel, J.: Outgoing longwave radiation and its diurnal variation from combined ERBE and Meteosat observations: 1. Estimating OLR from Meteosat data, Journal of Geophysical Research: Atmospheres (1984–2012), 96, 22 611–22 622, 1991.

Clerbaux, C., Boynard, A., Clarisse, L., George, M., Hadji-Lazaro, J., Herbin, H., Hurtmans, D., Pommier, M., Razavi, A., Turquety, S., et al.: Monitoring of atmospheric composition using the thermal infrared IASI/MetOp sounder, Atmospheric Chemistry and Physics, 9, 6041–6054, 2009.

Clerbaux, N., Dewitte, S., Gonzalez, L., Bertrand, C., Nicula, B., and Ipe, A.: Outgoing longwave flux estimation: Improvement of angular modelling using spectral information, Remote Sensing of Environment, 85, 389–395, 2003.

Clough, S., Shephard, M., Mlawer, E., Delamere, J., Iacono, M., Cady-Pereira, K., Boukabara, S., and Brown, P.: Atmospheric radiative transfer modeling: A summary of the AER codes, Journal of Quantitative Spectroscopy and Radiative Transfer, 91, 233–244, 2005.

Clough, S. A., Iacono, M. J., and Moncet, J.-L.: Line-by-line calculations of atmospheric fluxes and cooling rates: Application to water vapor, Journal of Geophysical Research: Atmospheres (1984–2012), 97, 15 761–15 785, 1992.

Crevoisier, C., Clerbaux, C., Guidard, V., Phulpin, T., Armante, R., Barret, B., Camy-Peyret, C., Chaboureau, J.-P., Coheur, P.-F., Crépeau, L., et al.: Towards IASI-New Generation (IASI-NG): impact of improved spectral resolution and radiometric noise on the retrieval of thermodynamic, chemistry and climate variables, Atmospheric Measurement Techniques Discussions, 6, 11 215–11 277, 2013.

Delamere, J., Clough, S., Payne, V., Mlawer, E., Turner, D., and Gamache, R.: A far-infrared radiative closure study in the Arctic: Application to water vapor, Journal of Geophysical Research: Atmospheres (1984–2012), 115, 2010.

Ellingson, R. G., Lee, H.-T., Yanuk, D. J., and Gruber, A.: A technique for estimating outgoing longwave radiation from HIRS radiance observations, Journal of Atmospheric and Oceanic Technology, 6, 706–711, 1989a.

Ellingson, R. G., Yanuk, D. J., and Gruber, A.: Effects of the choice of meteorological data on a radiation model simulation of the NOAA technique for estimating outgoing longwave radiation from satellite radiance observations, Journal of climate, 2, 761–765, 1989b.

Esposito, F., Grieco, G., Leone, L., Restieri, R., Serio, C., Bianchini, G., Palchetti, L., Pellegrini, M., Cuomo, V., Masiello, G., et al.: REFIR/BB initial observations in the water vapour rotational band: Results from a field campaign, Journal of Quantitative Spectroscopy and Radiative Transfer, 103, 524–535, 2007.

Feldman, D. R., Collins, W. D., Pincus, R., Huang, X., and Chen, X.: Far-infrared surface emissivity and climate, Proceedings of the National Academy of Sciences, 111, 16 297–16 302, 2014.

Goldberg, M., Ohring, G., Butler, J., Cao, C., Datla, R., Doelling, D., Gärtner, V., Hewison, T., Iacovazzi, B., Kim, D., et al.: The Global Space-Based Inter-Calibration System., Bulletin of the American Meteorological Society, 92, 2011.

Goody, R., Anderson, J., and North, G.: Testing climate models: An approach, Bulletin of the American Meteorological Society, 79, 2541–2549, 1998.

Green, P. D., Newman, S. M., Beeby, R. J., Murray, J. E., Pickering, J. C., and Harries, J. E.: Recent advances in measurement of the water vapour continuum in the far-infrared spectral region, Philosophical Transactions of the Royal Society A: Mathematical, Physical and Engineering Sciences, 370, 2637–2655, 2012.

Gruber, A.: Determination of the earth-atmosphere radiation budget from NOAA satellite data, Unknown, 1, 1977.

Gruber, A. and Winston, J.: Earth-atmosphere radiative heating based on NOAA scanning radiometer measurements, Bulletin of the American Meteorological Society, 59, 1570–1573, 1978.

Gruber, A., Ellingson, R., Ardanuy, P., Weiss, M., Yang, S., and Oh, S. N.: A comparison of ERBE and AVHRR longwave flux estimates, Bulletin of the American Meteorological Society, 75, 2115–2130, 1994.

Gube, M.: Radiation Budget Parameters at the Top of the Earth's Atmosphere from METEOSAT Data, Journal of Applied Meteorology, 21, 1907–1921, 1982.

Hanel, R. A., C. B. J. J. D. E. . S. R. E.: Exploration of the Solar System by Infrared Remote Sensing, Cambridge Univ. Press, 2003.

Hanel, R., Conrath, B., Kunde, V., Prabhakara, C., Revah, I., Salomonson, V., and Wolford, G.: The Nimbus 4 infrared spectroscopy experiment: 1. Calibrated thermal emission spectra, Journal of Geophysical Research, 77, 2629–2641, 1972.

Harries, J., Carli, B., Rizzi, R., Serio, C., Mlynczak, M., Palchetti, L., Maestri, T., Brindley, H., and Masiello, G.: The far-infrared earth, Reviews of Geophysics, 46, RG4004, 2008.

Harries, J. E., Brindley, H. E., Sagoo, P. J., and Bantges, R. J.: Increases in greenhouse forcing inferred from the outgoing longwave radiation spectra of the Earth in 1970 and 1997, Nature, 410, 355–357, 2001.

Haurwitz, F. and Kuhn, W. R.: The distribution of tropospheric planetary radiation in the Southern Hemisphere, Journal of Applied Meteorology, 13, 417–429, 1974.

Huang, X., Ramaswamy, V., and Schwarzkopf, M. D.: Quantification of the source of errors in AM2 simulated tropical clear-sky outgoing longwave radiation, Journal of Geophysical Research, 111, 2006.

Huang, X., Yang, W., Loeb, N. G., and Ramaswamy, V.: Spectrally resolved fluxes derived from collocated AIRS and CERES measurements and their application in model evaluation: Clear sky over the tropical oceans, Journal of Geophysical Research, 113, 2008.

Huang, X., Loeb, N., and Yang, W.: Spectrally resolved fluxes derived from collocated AIRS and CERES measurements and their application in model evaluation: 2. Cloudy sky and band-by-band cloud radiative forcing over the tropical oceans, Journal of Geophysical Research, 115, D21 101, 2010.

Huang, X., Cole, J. N., He, F., Potter, G. L., Oreopoulos, L., Lee, D., Suarez, M., and Loeb, N. G.: Longwave Band-By-Band Cloud Radiative Effect and Its Application in GCM Evaluation, Journal of Climate, 26, 450–467, 2013.

Huang, X., Chen, X., Potter, G. L., Oreopoulos, L., Cole, J. N., Lee, D., and Loeb, N. G.: A Global Climatology of Outgoing Longwave Spectral Cloud Radiative Effect and Associated Effective Cloud Properties, Journal of Climate, 27, 7475–7492, 2014.

Huang, Y., Ramaswamy, V., and Soden, B.: An investigation of the sensitivity of the clear-sky outgoing longwave radiation to atmospheric temperature and water vapor, Journal of Geophysical Research, 112, D05 104, 2007.

Illingworth, S., Remedios, J., and Parker, R.: Intercomparison of integrated IASI and AATSR calibrated radiances, Atmospheric Chemistry and Physics Discussions, 9, 8101–8119, 2009.

Kato, S. and Loeb, N. G.: Top-of-atmosphere shortwave broadband observed radiance and estimated irradiance over polar regions from Clouds and the Earth's Radiant Energy System (CERES) instruments on Terra, Journal of Geophysical Research: Atmospheres (1984–2012), 110, 2005.

King, N., Bower, K., Crosier, J., and Crawford, I.: Evaluating MODIS cloud retrievals with in situ observations from VOCALS-REx, Atmospheric Chemistry and Physics, 13, 191–209, 2013.

Larar, A., Smith, W., Zhou, D., Liu, X., Revercomb, H., Taylor, J., Newman, S., and Schlüssel, P.: IASI spectral radiance validation inter-comparisons: case study assessment from the JAIVEx field campaign, Atmos. Chem. Phys, 10, 411–430, 2010.

Lee, H., Gruber, A., Ellingson, R., and Laszlo, I.: Development of the HIRS outgoing longwave radiation climate dataset, Journal of Atmospheric and Oceanic Technology, 24, 2029–2047, 2007.

Lee, H.-T., Heidinger, A., Gruber, A., and Ellingson, R. G.: The HIRS outgoing longwave radiation product from hybrid polar and geosynchronous satellite observations, Advances in Space Research, 33, 1120–1124, 2004.

Lindfors, A. V., Mackenzie, I. A., Tett, S. F., and Shi, L.: Climatological diurnal cycles in clear-sky brightness temperatures from the High-Resolution Infrared Radiation Sounder (HIRS), Journal of Atmospheric and Oceanic Technology, 28, 1199–1205, 2011.

Loeb, N., Wielicki, B., Doelling, D., Smith, G., Keyes, D., Kato, S., Manalo-Smith, N., and Wong, T.: Toward optimal closure of the Earth's top-of-atmosphere radiation budget, Journal of Climate, 22, 748–766, 2009.

Loeb, N. G., Priestley, K. J., Kratz, D. P., Geier, E. B., Green, R. N., Wielicki, B. A., Hinton, P. O., and Nolan, S. K.: Determination of unfiltered radiances from the Clouds and the Earth's Radiant Energy System instrument, Journal of Applied Meteorology, 40, 822–835, 2001.

Loeb, N. G., Manalo-Smith, N., Kato, S., Miller, W. F., Gupta, S. K., Minnis, P., and Wielicki, B. A.: Angular Distribution Models for Top of Atmosphere Radiative Flux Estimation from the Clouds and

the Earths Radiant Energy System Instrument on the Tropical Rainfall Measuring Mission Satellite. Part I Methodology., Journal of applied meteorology, 42, 2003.

Maestri, T. and Rizzi, R.: A study of infrared diabatic forcing of ice clouds in the tropical atmosphere, Journal of geophysical research, 108, 4139, 2003.

Masiello, G., Serio, C., Esposito, F., and Palchetti, L.: Validation of line and continuum spectroscopic parameters with measurements of atmospheric emitted spectral radiance from far to mid infrared wave number range, Journal of Quantitative Spectroscopy and Radiative Transfer, 113, 1286–1299, 2012.

Minnis, P., Young, D. F., and Harrison, E. F.: Examination of the relationship between outgoing infrared window and total longwave fluxes using satellite data, Journal of climate, 4, 1114–1133, 1991.

Minnis, P., Young, D. F., Sun-Mack, S., Heck, P. W., Doelling, D. R., and Trepte, Q. Z.: CERES cloud property retrievals from imagers on TRMM, Terra, and Aqua, in: Remote Sensing, pp. 37–48, International Society for Optics and Photonics, 2004.

Mlynczak, M., Johnson, D., Bingham, G., Jucks, K., Traub, W., Gordley, L., and Harries, J.: The far-infrared spectroscopy of the troposphere (FIRST) project, in: Proc. SPIE, vol. 5659, pp. 81–87, 2004.

Mlynczak, M., Johnson, D., Latvakoski, H., Jucks, K., Watson, M., Kratz, D., Bingham, G., Traub, W., Wellard, S., Hyde, C., et al.: First light from the Far-Infrared Spectroscopy of the Troposphere (FIRST) instrument, Geophysical research letters, 33, L07 704, 2006.

Ohring, G., Gruber, A., and Ellingson, R.: Satellite determinations of the relationship between total longwave radiation flux and infrared window radiance, Journal of climate and applied meteorology, 23, 416–425, 1984.

Palchetti, L., Bianchini, G., Carli, B., Cortesi, U., and Bianco, S. D.: Measurement of the water vapour vertical profile and of the Earth's outgoing far infrared flux, Atmospheric Chemistry and Physics, 8, 2885–2894, 2008.

Phillips, N., Susskind, J., and McMillin, L.: Results of a joint NOAA/NASA sounder simulation study, Journal of Atmospheric and Oceanic Technology, 5, 44–56, 1988.

Priestley, K., Wielicki, B., Green, R., Haeffelin, M., Lee, R., and Loeb, N.: Early radiometric validation results of the CERES Flight Model 1 and 2 instruments onboard NASA'S Terra Spacecraft, Advances in Space Research, 30, 2371–2376, 2002.

Raschke, E., Vonder Haar, T. H., Bandeen, W. R., and Pasternak, M.: The Annual Radiation Balance of the Earth-Atmosphere System During 1969-70 from Nimbus 3 Measurements., Journal of Atmospheric Sciences, 30, 341–364, 1973.

Rizzi, R. and Mannozzi, L.: Preliminary results on the planetary emission between 100 and 600 cm -1, REFIR Radiation Explorer in the Far Infrared Final Rep ENV4 CT6, 344, 77–88, 2000.

Rosenfeld, D., Cattani, E., Melani, S., and Levizzani, V.: CONSIDERATIONS ON DAYLIGHT OPERATION OF 1.6-VERSUS 3.7-um CHANNEL ON NOAA AND METOP SATELLITES, Bulletin of the American Meteorological Society, 85, 873–881, 2004.

Saunders, R., Hocking, J., Rundle, D., Rayner, P., Matricardi, M., Geer, A., Lupu, C., Brunel, P., and Vidot, J.: RTTOV-11 Science and validation report, NWP SAF Report, 32, 2013.

Schmetz, J. and Liu, Q.: Outgoing longwave radiation and its diurnal variation at regional scales derived from Meteosat, Journal of Geophysical Research: Atmospheres (1984–2012), 93, 11 192–11 204, 1988.

Shephard, M., Clough, S., Payne, V., Smith, W., Kireev, S., and Cady-Pereira, K.: Performance of the line-by-line radiative transfer model (LBLRTM) for temperature and species retrievals: IASI case studies from JAIVEx, Atmospheric Chemistry and Physics, 9, 7397–7417, 2009.

Simeoni, D., Astruc, P., Miras, D., Alis, C., Andreis, O., Scheidel, D., Degrelle, C., Nicol, P., Bailly, B., Guiard, P., et al.: Design and development of IASI instrument, in: Optical Science and Technology, the SPIE 49th Annual Meeting, pp. 208–219, International Society for Optics and Photonics, 2004.

Sohn, B.-J. and Bennartz, R.: Contribution of water vapor to observational estimates of longwave cloud radiative forcing, Journal of Geophysical Research: Atmospheres (1984–2012), 113, 2008.

Sun, F., Goldberg, M. D., Liu, X., and Bates, J. J.: Estimation of outgoing longwave radiation from Atmospheric Infrared Sounder radiance measurements, Journal of Geophysical Research, 115, 2010.

Thomas, S. and Priestley, K.: CERES FM1 - FM6 Instrument Update., Spring 2014 CERES Science Team Meeting. April 22-24. Hampton, VA, 2014.

Turner, D. D., Tobin, D., Clough, S. A., Brown, P. D., Ellingson, R. G., Mlawer, E. J., Knuteson, R. O., Revercomb, H. E., Shippert, T. R., Smith, W. L., et al.: The QME AERI LBLRTM: A closure experiment for downwelling high spectral resolution infrared radiance., Journal of the atmospheric sciences, 61, 2004.

Wang, C., Yang, P., Dessler, A., Baum, B. A., and Hu, Y.: Estimation of the cirrus cloud scattering phase function from satellite observations, Journal of Quantitative Spectroscopy and Radiative Transfer, 138, 36–49, 2014.

Wielicki, B., Barkstrom, B., Harrison, E., Lee III, R., Louis Smith, G., and Cooper, J.: Clouds and the Earth's Radiant Energy System (CERES): An earth observing system experiment, Bulletin of the American Meteorological Society, 77, 853–868, 1996.

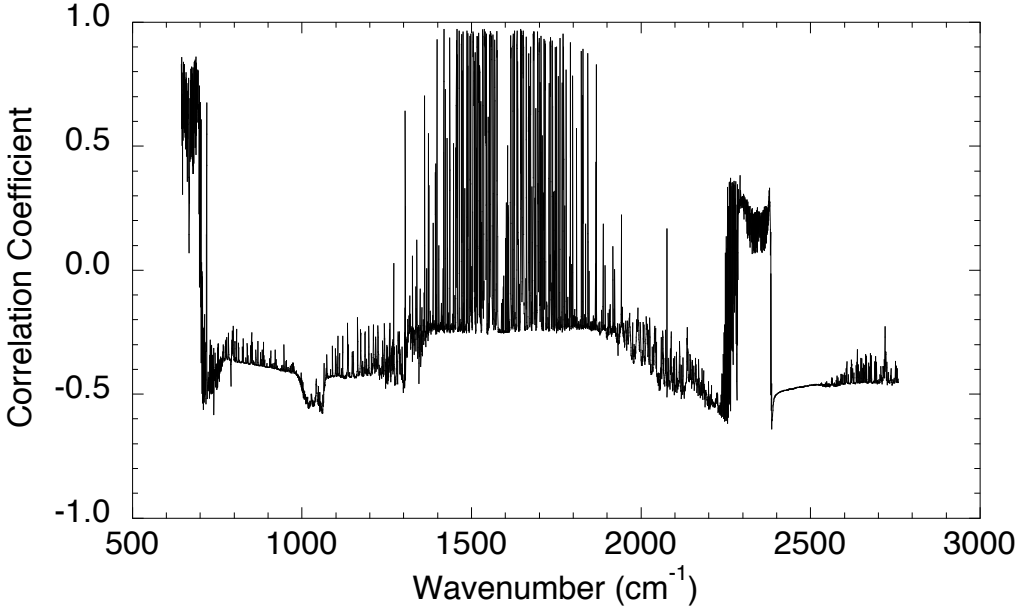

Figure 1. Linear correlation coefficients between the radiance at 25.25 cm^{-1} and the rest of the spectrum. Data is simulated by the LBLRTM from Phillips Soundings.

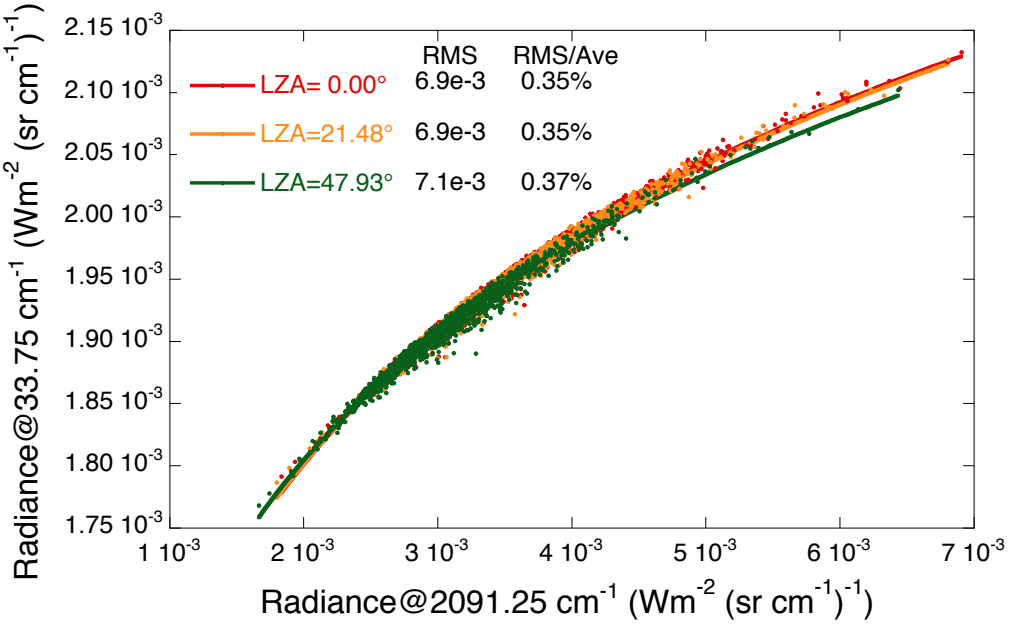

Figure 2. Relationship of radiances at 33.75 cm^{-1} and 2091.25 cm^{-1} simulated by LBLRTM from Phillips Soundings, where the scatter points and fitting curve are based on data for local zenith angles (LZA) of 0° (red), 21.48° (orange), and 47.93° (green), respectively. Units are $Wm^{-2}sr^{-1}(cm^{-1})^{-1}$.

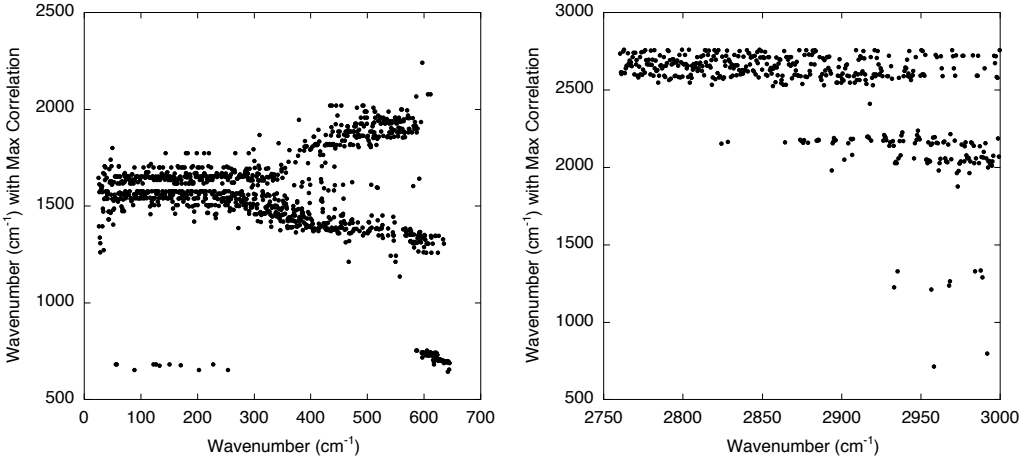

Figure 3. The wavenumbers of IASI observed radiance spectrum (y-axis) that show empirically the maximum correlation coefficients for the FIR (left) and NIR (right) wavenumbers (x-axis), based on a log-log transformation.

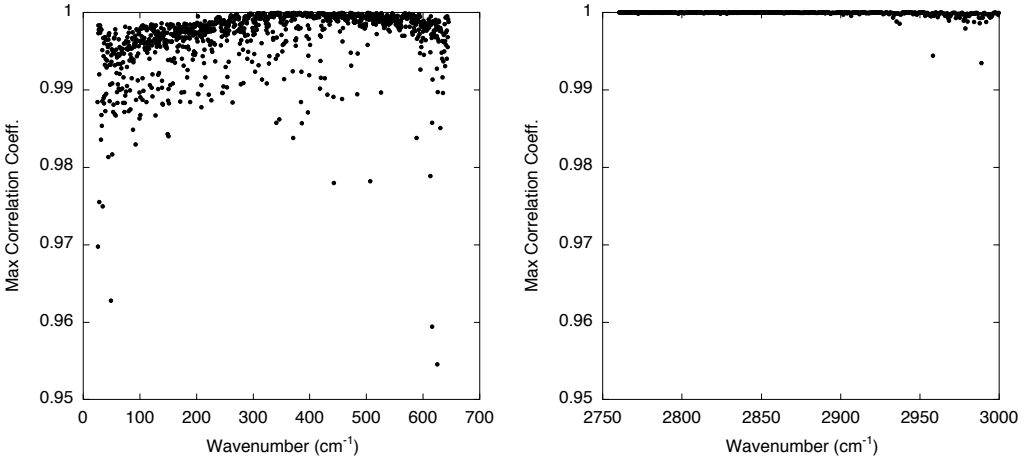

Figure 4. The maximum correlation coefficients between wavenumbers in the FIR (left) and NIR (right) and the corresponding predictor wavenumbers shown in Figure 3.

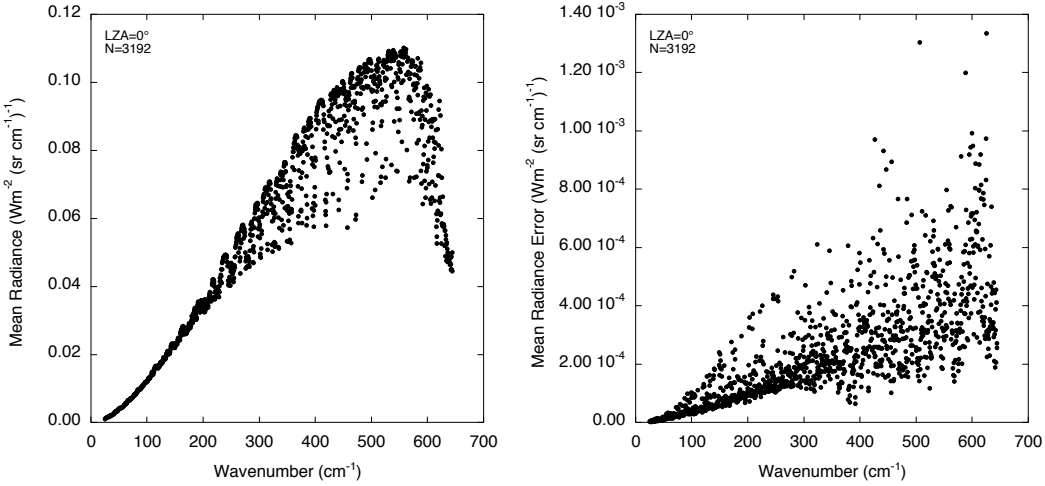

Figure 5. The mean FIR radiance spectrum based on all LBLRTM simulations performed with the 3192 radiosonde profiles (left), and the spectral radiance estimation errors (regression rms errors) associated with them (right). All simulations shown are for a local zenith angle of 0 °.

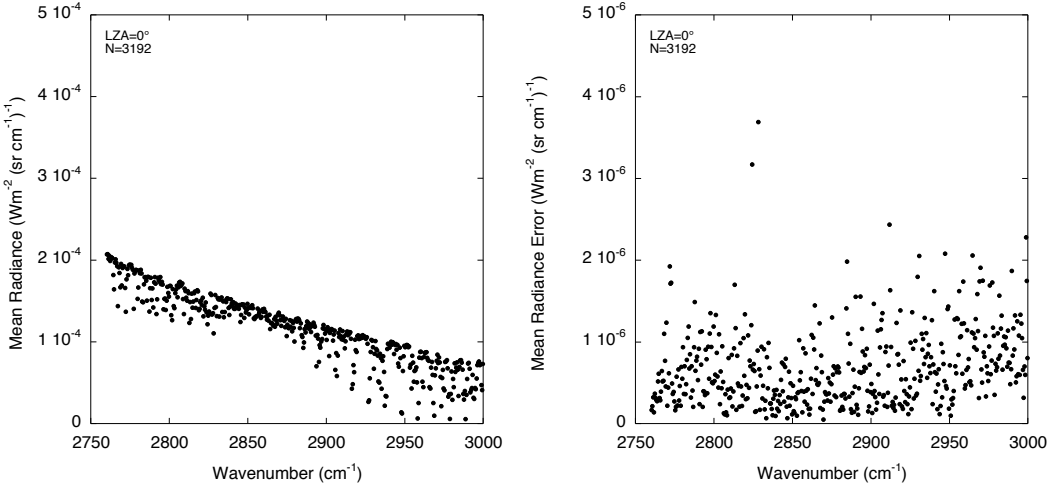

Figure 6. The mean NIR radiance spectrum based on all LBLRTM simulations performed with the 3192 radiosonde profiles (left), and the spectral radiance estimation errors (regression rms errors) associated with them (right). All simulations shown are for a local zenith angle of 0 °.

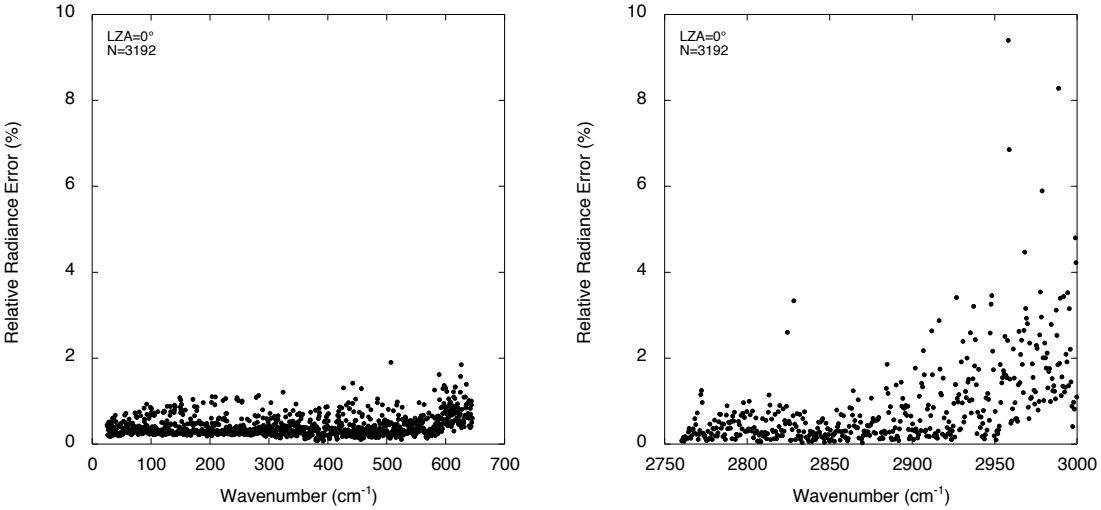

Figure 7. Relative radiance estimation error for the FIR (left) and the NIR (right) regions. Calculated from the root mean square values of the radiance errors divided by the mean radiance spectrum (the right and left plots of Figures 5 and 6 respectively).

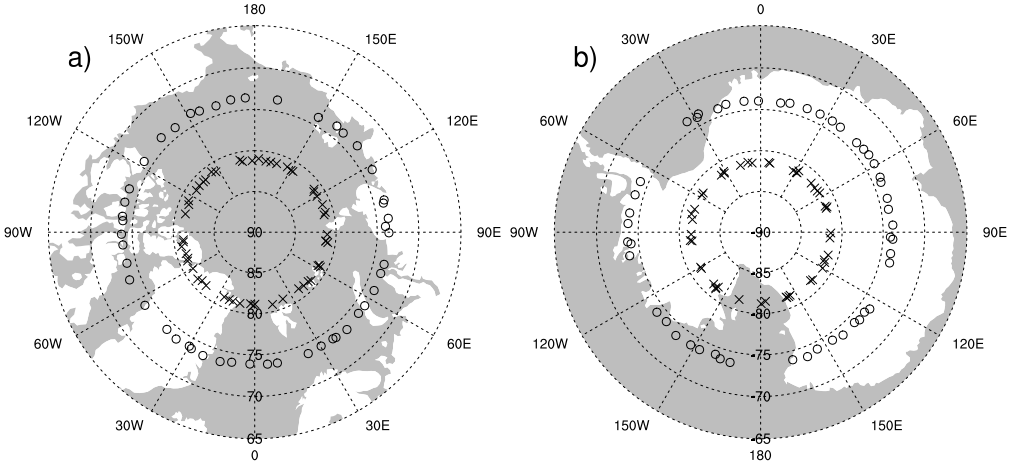

Figure 8. Locations of nearest nadir viewing SNOs, chosen as described in section 2.4 between Metop-A and Terra (inner crosses) and Aqua (outer circles) for a) the Arctic, and b) Antarctic, for 2012.

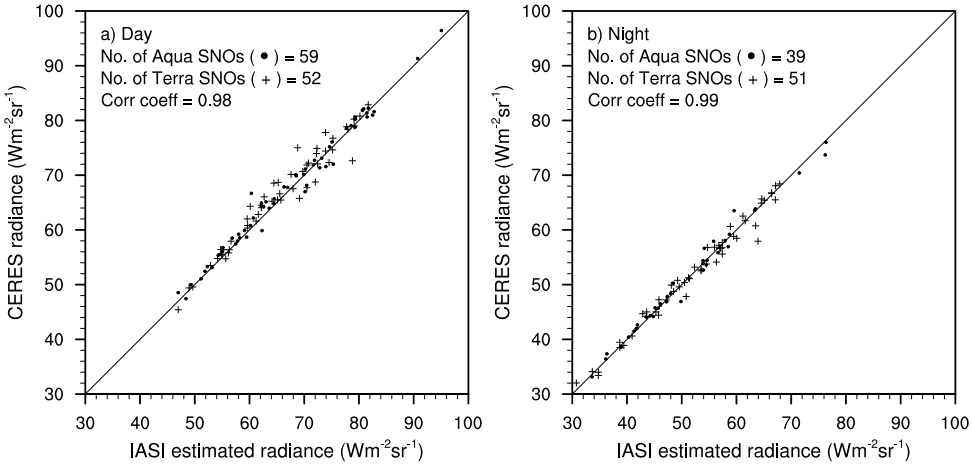

Figure 9. Absolute values of INLR constructed from IASI on Metop-A against CERES measurements for both the Terra and Aqua satellites at closest SNO events for 2012 for a) day, and b) night.

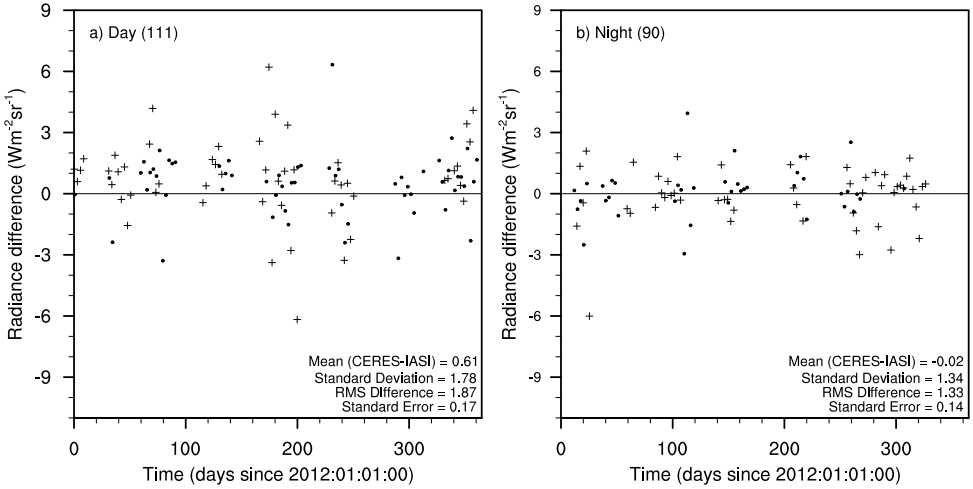

Figure 10. Time series of INLR bias at SNOs between CERES and IASI for 2012 for a) day and b) night. CERES measurements from Terra are marked with crosses and those from Aqua are shown as dots. Standard error is the standard deviation divided by the square root of the total number of points.

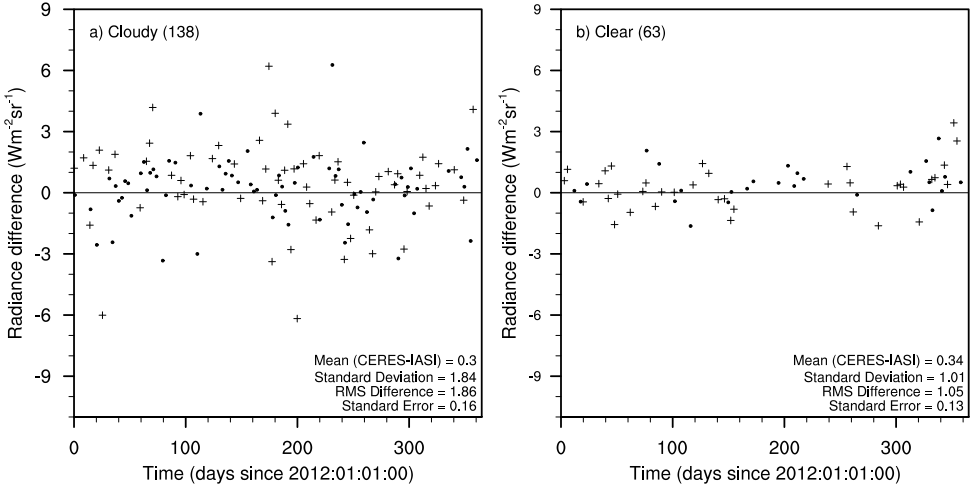

Figure 11. Time series of INLR bias at SNOs between CERES and IASI for 2012 for a) cloudy and b) clear pixels, as identified by the MODIS near infrared 3.7 μm channel. CERES measurements from Terra are marked with crosses and those from Aqua are shown as dots. Standard error is the standard deviation divided by the square root of the total number of points.

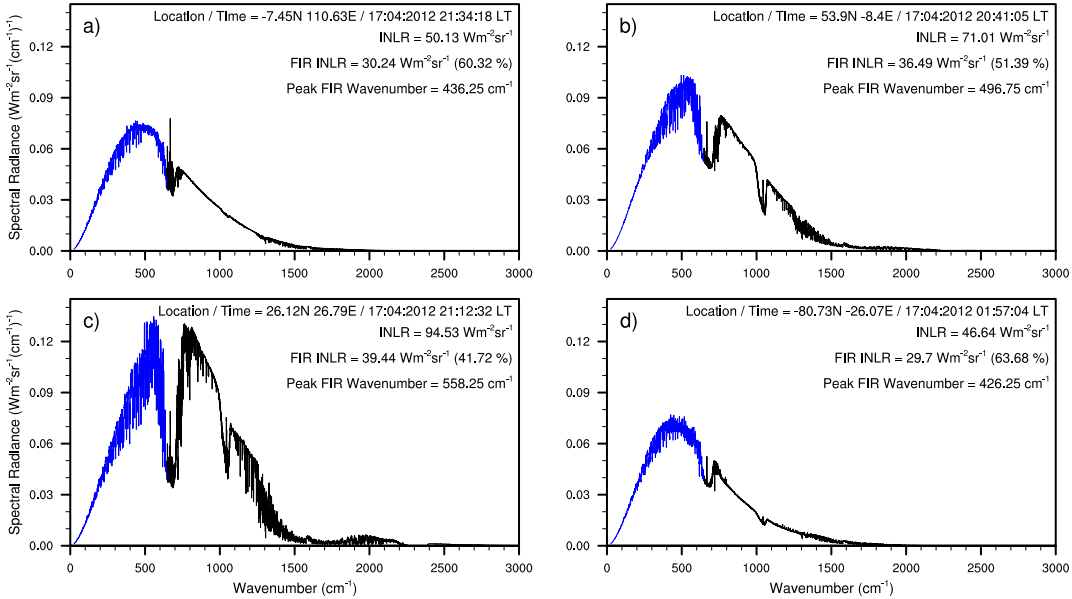

Figure 12. The total outgoing longwave spectral radiance (25.25 - 2999.75 cm^{-1}) constructed from IASI measurements (black) and estimated far infrared radiances (blue) for 4 instantaneous scenes over: a) tropical equatorial land, b) midlatitude land, c) the Sahara desert, and d) Antarctica. All are night-time scenes from the 17th April 2012.

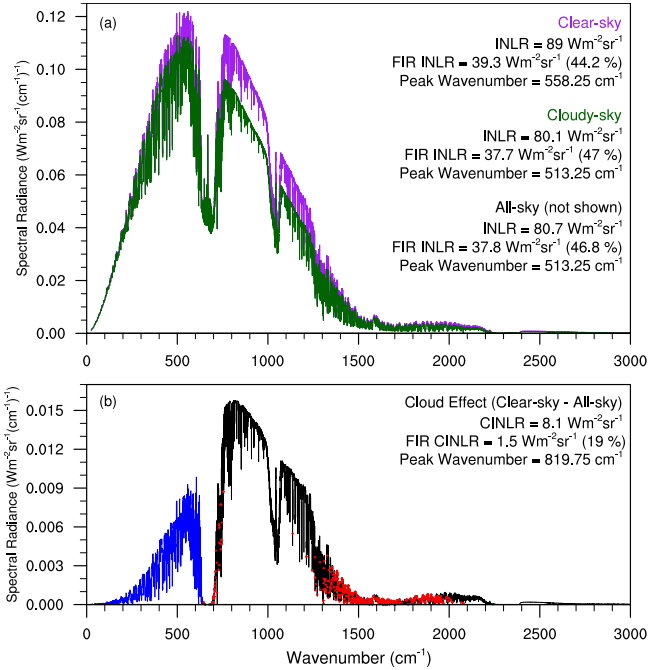

Figure 13. The outgoing longwave spectral radiance constructed from IASI data globally averaged for: a) clear (purple) and cloudy (green) pixels. Numbers in parentheses are the fractional FIR contributions to the total LW broadband INLR. The all-sky curve is between the clear and cloudy curves but is not plotted for clarity. b) The difference between the clear-sky and all-sky spectrum's constructed from IASI measurements (black) and estimated far infrared radiances (blue) from predictor wavelengths in the mid infrared with the highest correlations (red dots). The number in parentheses is the fractional contribution of the FIR INLR (FIR CINLR) to the total INLR (CINLR). Data is the area weighted mean of April 2012.

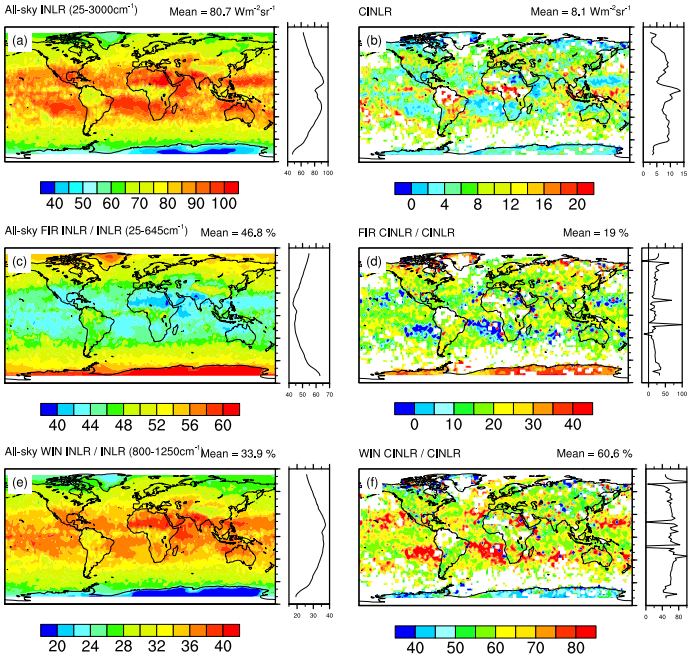

Figure 14. INLR and CINLR maps created from all April 2012 pixels binned to a 2.5 by 2.5 grid and averaged. Zonal means are shown to the right of each map. On the left hand side is all-sky: a) INLR, c) FIR as a percentage of INLR, e) the window region as a percentage of INLR. On the right is CINLR (clear-sky - all-sky) for: b) INLR, d) the percentage of CINLR that is FIR, f) the percentage of CINLR that is in the window region. Note that the colour scales are different for every panel. Missing data is shown in white.

Table 1. Instantaneous biases between CERES and IASI INLR at SNO events with standard errors. Standard errors are the standard deviations divided by the square root of the total number of points. Units are $Wm^{-2}sr^{-1}$. Figures in brackets are relative differences between the bias and the mean radiation measured by both CERES and IASI.

	All times	Day	Night
Both	0.33 ±0.11 (0.53%)	0.61 ±0.17 (0.95%)	-0.02 ±0.14 (0.01%)
Aqua	0.33 ±0.14 (0.57%)	0.48 ±0.20 (0.78%)	0.11 ±0.19 (0.25%)
Terra	0.32 ±0.18 (0.50%)	0.76 ±0.28 (1.15%)	-0.12 ±0.2 (-0.17%)
Clear	0.34 ±0.13 (0.50%)	0.84 ±0.17 (0.31%)	-0.21 ±0.13 (-0.35%)
Cloudy	0.30 ±0.16 (0.51%)	0.48 ±0.23 (0.78%)	0.06 ±0.2 (0.15%)